Embedding nano-silicon in graphene nanosheets by plasma assisted milling for high capacity anode materials in lithium ion batteries

Wei Sun [a], Renzong Hu [a], Hui Liu [a], Meiqin Zeng [a], Lichun Yang [a], Haihui Wang [b], Min Zhu [a,*]

[a] School of Materials Science and Engineering, South China University of Technology, Key Laboratory of Advanced Energy Storage Materials of Guangdong Province, Guangzhou 510641, China
[b] School of Chemistry & Chemical Engineering, South China University of Technology, Guangzhou 510641, China

HIGHLIGHTS

- Discharge-plasma assisted milling is used to produce a nano-Si/graphene nanosheets composite.
- Nano-Si are homogeneously embedded in the *in-situ* formed graphene nanosheets.
- The graphene nanosheets much enhance the cycling stability and rate capability.
- Full cell with good performance demonstrates a satisfying utilization of the composite.

ARTICLE INFO

ABSTRACT

The lithium storage performance of silicon (Si) is improved substantially by forming composite of nano-Si particles embedded homogeneously in graphene nanosheets (GNs) using a simple discharge plasma assisted milling (P-milling) method. The synergistic effect of the rapid heating of the plasma and the mechanical ball mill grinding with nano-Si as nanomiller converted the graphite powder to GNs with the integration of nano-Si particles in the *in-situ* formed GNs. This composite structure inhibits the agglomeration of nano-Si and improves electronic conductivity. The cycling stability and rate capability are enhanced, with a stable reversible capacity of 976 mAhg^{-1} at 50 mAg^{-1} for the P-milled 20 h nano-Si/GNs composite. A full cell containing a commercial LiMn$_2$O$_4$ cathode is assembled and demonstrated a satisfying utilization of the P-milled nano-Si/GNs composite anode with stable working potential. This composite shows promise for application in lithium ion batteries.

1. Introduction

Lithium ion batteries (LIBs) are important power sources in a variety of applications, including portable electronic devices and home electronics, and their use is now being expanded to EV. These applications require LIBs with high energy density [1,2]. Much effort has therefore been devoted to developing higher capacity anode materials to substitute currently used graphite anodes with low theoretical capacity limitation (372 mAhg^{-1}) [3,4]. Many metals and semiconductor materials, which can react reversibly with lithium, such as Al, Si, Ge, Sn, Sb, have therefore attracted great interest as alternatives [5]. Among these, Si-based materials are the most promising alternative because of their low cost, natural abundance and especially their highest theoretical capacity (4200 mAhg^{-1}, corresponding to the Li$_{22}$Si$_5$ alloy) [6–8]. However, poor cycleability, which is caused by structural failure and pulverization because of the huge volume change (>300%) of Si during Li$^+$ insertion and removal, hinders its practical application [9]. In addition, the low intrinsic electronic conductivity of Si usually leads to an inferior rate of performance and lower reversible capacity.

Much effort has been made to solve these problems. The most common approach is to prepare composites with nano-Si particles/clusters dispersed uniformly in a carbonaceous matrix. The matrix is able to buffer the large volume expansion and enhance Si conductivity during cycling [10–13]. Different kinds of carbonaceous materials combined with nano-Si, such as graphite [14–16], pyrolysed carbon [17], mesoporous carbon [18], and carbon nanotubes [19] have been investigated using this approach. A new type of carbonaceous material, graphene nanosheets (GNs, 3–6 nm in thickness) [20], possess superior electrical conductivity, good flexibility, and chemical stability [21,22]. They are therefore a
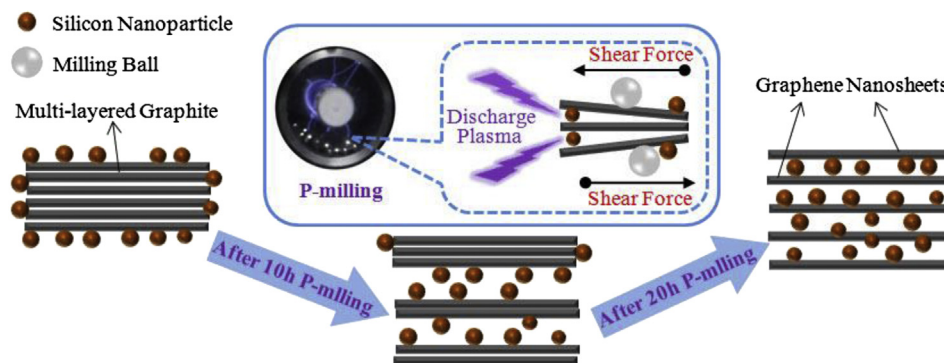
Fig. 1. Schematic illustration of nano-Si/GNs composites preparation by P-milling.

suitable matrix or additive for Si-based composite anode materials [23]. GNs have been produced by several techniques, including the mechanical peeling-off of graphite [24,25], chemical vapor deposition (CVD) [24,26], and chemical or thermal reduction from graphite oxide [27,28]. However, for Si-based anode materials, many difficulties still exist in the utilization of graphene by the mechanical peeling-off of graphite and CVD which may be complex and expensive for mass production. Widely reported preparation routes for Si/GNs composites based on graphite oxide require harsh conditions such as strong oxidizing and reducing reagents, high temperature, and precise times and reactant ratios, leading to a laborious and time-consuming preparation process [24,29,30]. It is also difficult to obtain highly dispersed nano-Si particles in the as-prepared GNs, which is a key factor in achieving good performance [27,31], by simply mechanical blending.

Dielectric barrier discharge plasma assisted milling (P-milling) is different from conventional mechanical milling in that it has a synergistic effect of the rapid heating of the discharge plasma and the impact stress of mechanical milling. This method has been used successfully to prepare Sn/graphite composite anodes for LIBs [32], where Sn particles could be refined rapidly and be well-dispersed in the graphite matrix. This leads to an enhanced cyclic performance of the LIB anode. GNs have not been synthesized in P-milled Sn−C composite materials [32,33]. Here, we report on a one-step synthesis method for the efficient production of nano-Si/GNs composites on a large scale by P-milling. We have used rigid nano-Si particles as nanomillers to peel GNs from microsized graphite *in-situ* in the P-milling process. The presence of GNs, as well as the high-dispersion state of nano-Si particles in the GN matrix enhances the cycling stability and rate capability of the composite electrodes.

2. Experimental

2.1. Material preparation

Nano-Si powder (99.9% purity, 50−100 nm in size, Xuzhou Jie-chuang New Material Technology Co., Ltd) and natural graphite (99.9% purity, 30 μm in size, Shanghai Colloid Chemical Plant) were used as raw materials. A 30:70 mass ratio of nano-Si to graphite powder was mixed and placed in a stainless steel vial with stainless steel balls. The mass ratio of ball to powder was 50:1. The powder mixture was treated by P-milling for 5, 10 and 20 h without pre-treatment to produce nano-Si/graphite composite samples termed P-5h, P-10h, and P-20h, respectively. Milling was conducted under pure argon atmosphere with a vibration type ball mill (milling cylinder vibration with double amplitude of 7 mm and frequency of 24 Hz). Details of the P-milling have been described previously [32,34,35]. For comparison, nano-Si powder was mixed with

graphite by manual grinding in air to obtain a nano-Si/graphite mixture sample termed P-0h.

2.2. Material characterization

Materials were characterized using an XRD (Philips) with Cu-Kα radiation, a laser Raman spectrometer (Horiba) with 632.81 nm laser, a field emission SEM (Carl Zeiss Supra 40), and a TEM (JEOL
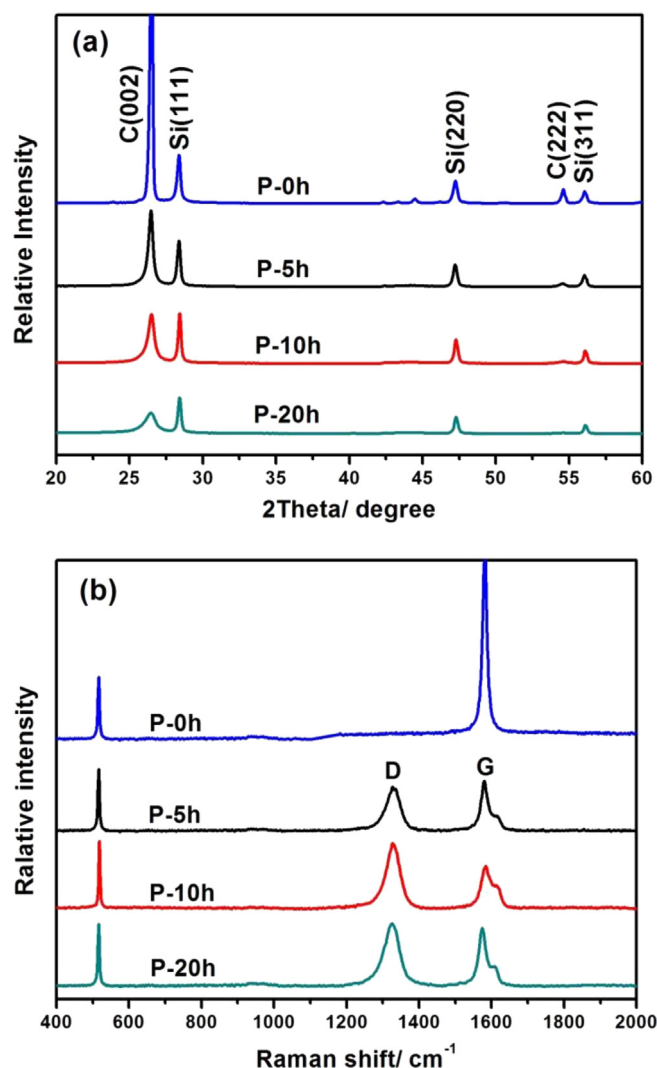

Fig. 2. (a) XRD and (b) Raman spectra for P-5h, P-10h, and P-20h nano-Si/graphite composites. Nano-Si/graphite P-0h mixture provided for comparison.

Table 1
Nanostructure evolution of P-0h, P-5h, P-10h, and P-20h samples from XRD, Raman, and BET results. (d_{002}: interlayer spacing of (002) plane, L_c: crystalline parameter calculated from peak position and half-height width of (002) reflection).

Sample	2θ (°)	d_{002}(nm)	L_c (nm)	Number of stacking layers	I_D/I_G	Specific surface area (m^2 g^{-1})
P-0h	26.5098	0.3359	49.5	147	0	5.29
P-5h	26.4693	0.3365	27.8	83	0.93	37.94
P-10h	26.4542	0.3366	20.1	59	1.36	41.91
P-20h	26.4211	0.3371	7.2	21	1.49	81.17

JEM-2100) operating at 200 kV. For TEM observations, the sample was prepared by dispersion of the as-prepared powders on Cu grids. The specific surface area of the sample was determined using the BET method with gas reaction controller (American Advanced Materials Corporation) by nitrogen absorption. DSC and TGA were carried out under oxygen on a TGA/DSC1 (Mettler-Toledo) with heating rate of 20 °Cmin^{-1}.

2.3. Electrochemical measurements

The electrochemical performance of the samples was investigated using CR2016 coin-type cells assembled in an argon-filled glove box. The working electrode consisted of 80 wt% active material, 10 wt% conductivity agent (Super-P), and 10 wt% carboxymethyl cellulose sodium salt dissolved in distilled water as a binder. The amount of active material loaded on the electrodes was 1.3 ~ 1.5 mg cm^{-2}. Lithium metal foils were used as counter and reference electrodes in the half cells. A coin-type full cell was assembled using the as-prepared composites and LiMn$_2$O$_4$ (Shun Wo New Power Electronics (Shenzhen) Ltd) as anode and cathode, respectively. The electrodes were separated by separators (Teklon@Gold LP) in the cells. The electrolyte was LiPF$_6$ (1 M) in a mixture of EC/diethylene carbonate (DEC)/ethyl methyl carbonate (EMC) (1:1:1 v:v:v) (Shanshan Tech Co., Ltd).

Galvanostatic charge and discharge tests of half and full cells were carried out using CT2001A (LAND, China) battery testers. Half
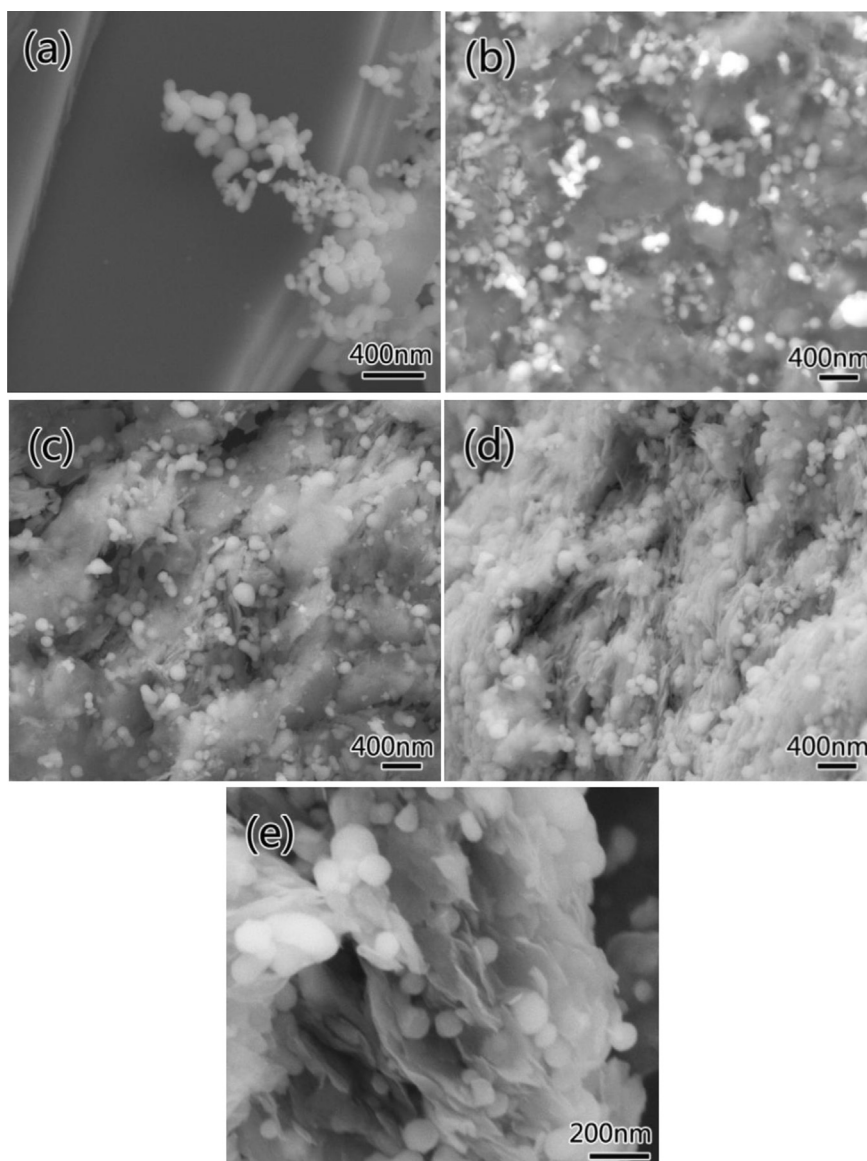
Fig. 3. SEM micrographs of (a) P-0h, (b) P-5h, (c) P-10h, (d) and (e) P-20h samples, showing morphology change from graphite to GNs.
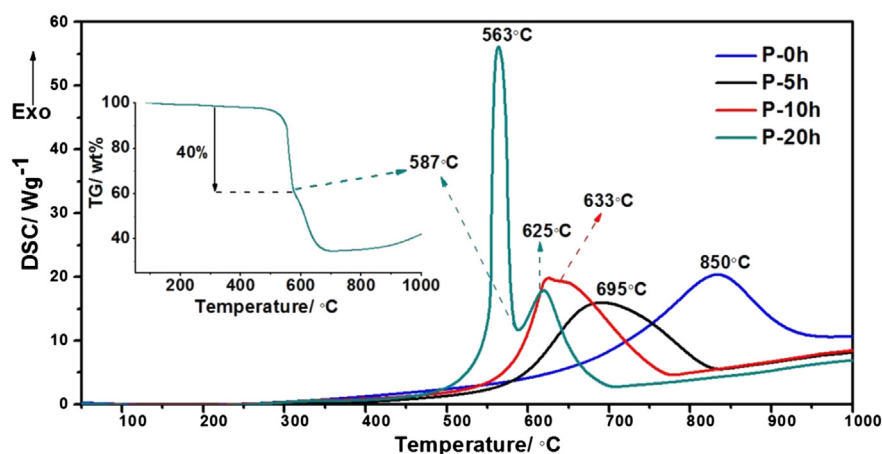
Fig. 4. DSC curves of P-0h, P-5h, P-10h, P-20h samples and TG curve (inset) for P-20h under oxygen atmosphere and heating rate of 20 °Cmin^{-1}.

cells were tested at various current rates from 0.01 to 1.5 V, while the full cell was tested at 400 mAg^{-1} from 2.5 to 4.5 V. The current density and capacity were based on the weight of active material (Si or Si/GNs composites) without conductivity agent and binder. CV was conducted with a Gamry electrochemical system from 0 to 2.0 V versus Li/Li$^+$ at a scanning rate of 0.3 mVs^{-1}. Impedance spectra were carried out by applying a 5 mV amplitude signal range from 1 MHz to 0.1 Hz. Current-voltage (I–V) curves were obtained by a linear voltage swap from −1 to 1 V for the P-20h composite

bulk sample and from 6 to 8 V for the Si bulk sample. Both bulk samples were compressed by powder at a pressure of 90 kN. All electrochemical tests were carried out at ambient temperature.

3. Results and discussion

The synthesis of nano-Si/GNs composites by P-milling is illustrated schematically in Fig. 1. A nanostructure evolution of nano-Si/graphite composites during P-milling is expected to occur because
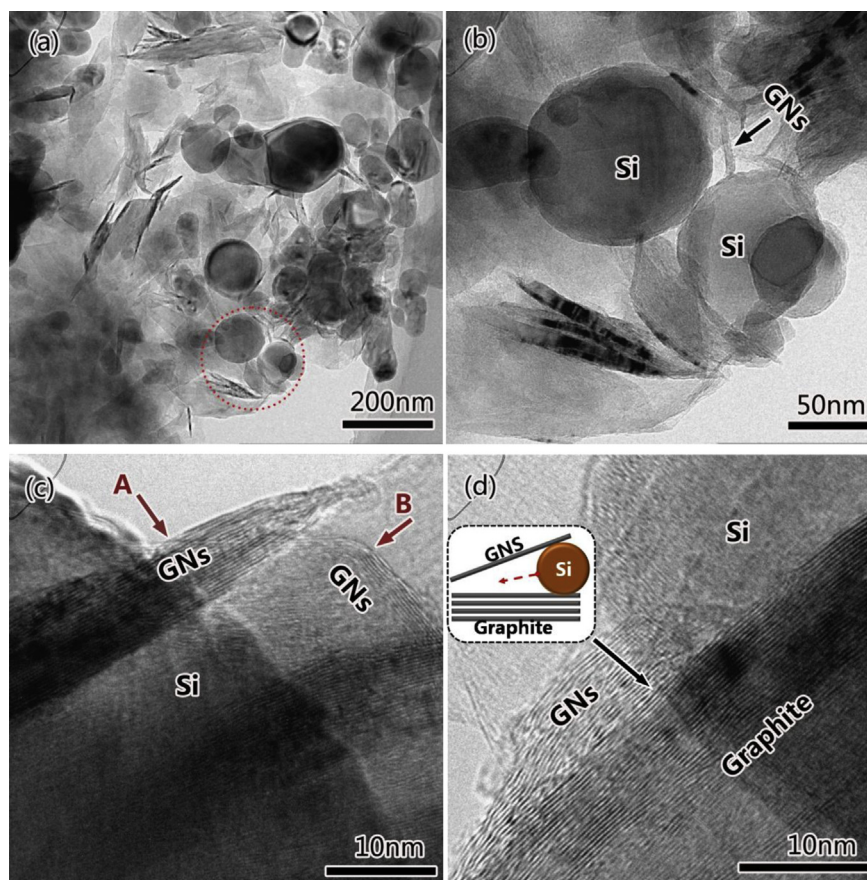

Fig. 5. (a) Typical TEM micrograph of P-20h nano-Si/GNs composite sample; (b) large magnification TEM micrograph of zone delineated by dotted circle in (a); (c, d) high resolution TEM micrographs of P-20h sample; inset in (d) shows schematic of the cutting effect of the nano-Si particle.

of the synergistic effect from the milling impact stress and the rapid heating of the discharge plasma. The impact force of the milling balls, and in particular the cutting effect of the hard nano-Si particles on the graphite, accelerates the mechanical peeling of the graphite layers to form GNs during milling. The discharge plasma leads to rapid heating and even to thermal explosions [32] which results in a thermal expansion of the graphite and causes the peeling off of graphite to form GNs. A nano-Si/GNs composite therefore formed with the unique structure of nano-Si particles embedded in the GNs. As shown in Fig. 2, the microstructure of the nano-Si/GNs composite was influenced by the P-milling time and

would have a significant impact on their specific capacity and cycleability for lithium storage.

Fig. 2a shows the XRD spectra of the nano-Si/graphite composite after P-milling for different times. Sharp diffraction peaks of graphite and Si exist for sample P-0h, indicating their perfect crystalline nature before milling. After P-milling, the main diffraction peak of graphite (002) broadens and weakens with increasing P-milling time. Based on the peak profile analysis using a Scherrer equation [36], the crystalline parameters of graphite in the different nano-Si/graphite composites were obtained and are summarized in Table 1. The graphite particle size has been reduced in the c-
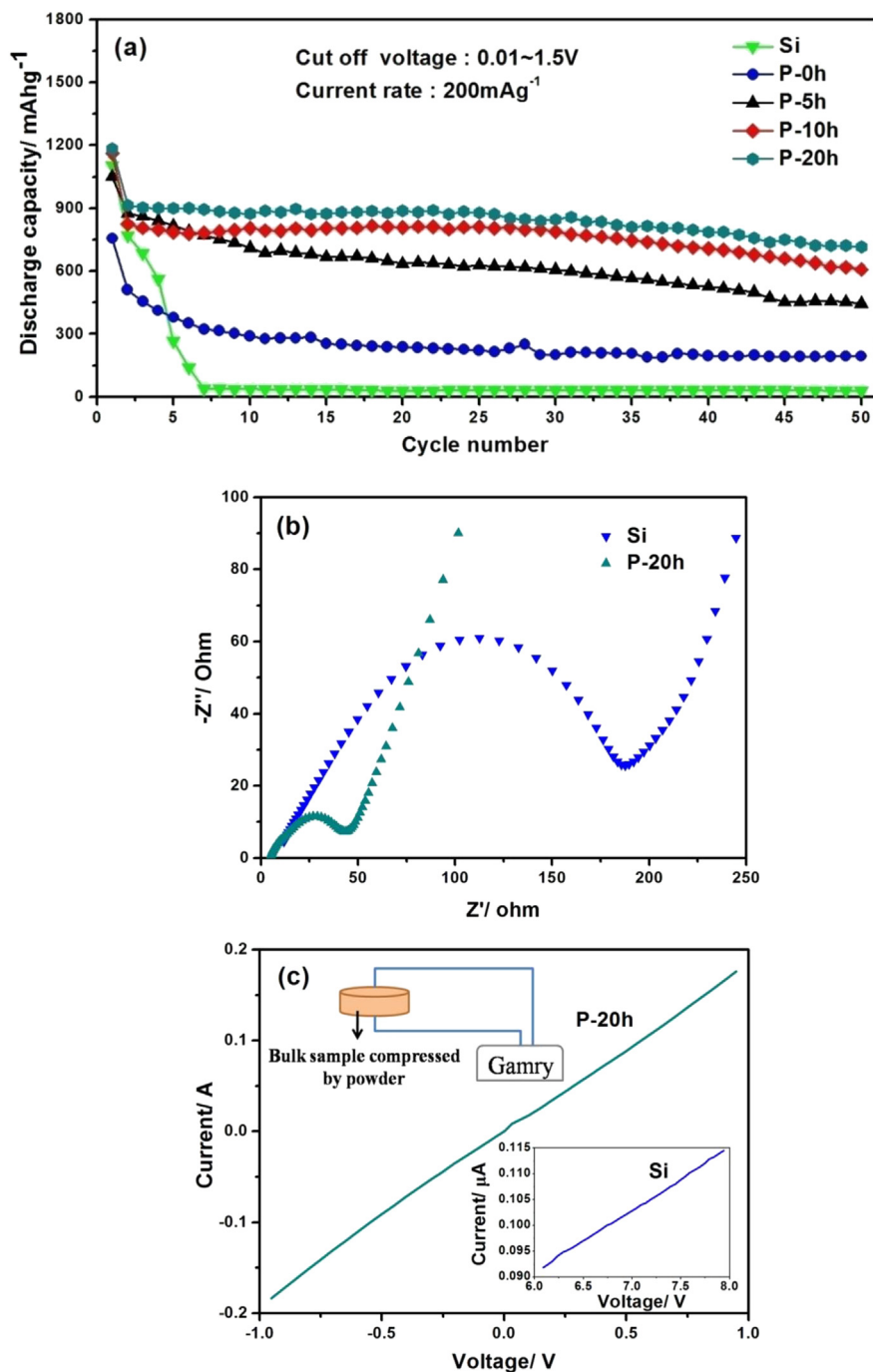

Fig. 6. (a) Cycling performance of half cells with nano-Si and P-0h, P-5h, P-10h, and P-20h samples at 200 mAg^{-1} between 0.01 and 1.5 V. (b) Impedance spectra of nano-Si and P-20h nano-Si/GNs composite. (c) Current-voltage $(I–V)$ curves of P-20h composite bulk sample and Si bulk sample (right inset).

direction. Based on the lattice spacing of the graphite (002) plane, the average number of stacking layers for GNs in the P-milled composites is calculated to be 59 and 21 for P-10h and P-20h, respectively. Graphene nanosheets containing nano-Si can therefore be obtained by P-milling. Compared with the significant structural changes in graphite during P-milling, the main peaks of Si (111) and Si (220) show no obvious changes. This could be attributed to its nanocrystalline nature (50—100 nm in size) and high hardness.

Significant changes in graphite structure during P-milling were also revealed by Raman spectra, as shown in Fig. 2b. Three main peaks exist at approximately 518 cm^{-1}, 1338 cm^{-1}, and 1582 cm^{-1} for the P-5h, P-10h, and P-20h samples, respectively. These are induced by the silicon, D and G bands of carbon, respectively. The D band corresponds to disordered carbon, edges and other defects, while the G band originates from the ordered sp^2 bonded carbon [37—39]. The intensity of the D band of the P-5h, P-10h, and P-20h samples increased while that of the G band decreased as the P-milling time increased. An I_D/I_G intensity ratio of 0.93, 1.36, and 1.49 existed for the P-5h, P-10h, and P-20h samples respectively, as given in Table 1. These results again indicate that there is a significant reduction in size of the graphite along the c-direction and an accumulation of defects from the synergistic interaction of the cutting by the nano-Si particles, the rapid plasma heating and the mechanical milling impact stress of the P-milling. The composite specific surface area therefore increases with prolonged milling as shown in Table 1.

The SEM micrographs in Fig. 3 show the morphology change from graphite to GNs. The nano-Si particles of the manually prepared sample (P-0h, Fig. 3a) are spherical with a size range of 50—100 nm, while graphite has a typical bulk layer structure. The nano-Si particles were agglomerated and dispersed randomly on the graphite surfaces. As P-milling proceeded, large graphite particles were cut into small flakes and thin sheets. For the P-5h sample (Fig. 3b), the microsized graphite was reduced to the nanoscale and was well-mixed with nano-Si particles in two forms: one in which the nano-Si particles were distributed randomly on the graphite surface and the other in which the nano-Si particles were embedded in the nanosized graphite layer. With an increase in P-milling time to 10 and 20 h (Fig. 3c and d, respectively) the graphite layer became thinner and the nano-Si particles were more uniformly distributed inside the nanoscale graphite layers. For the P-20h sample, the graphite layers thinned and became GNs with thickness less than 10 nm. The enlarged SEM micrograph in Fig. 3e shows that the gaps among the GNs are filled with nano-Si particles and that a large number of nanosized free spaces exist between the GNs and the nano-Si particles. The nanosized free spaces could accommodate a volume change of the inner active nano-Si particles during Li alloying and dealloying. It is expected that a conductive network and buffer matrix can be achieved for the Li—Si reactions with this unique structure of nano-Si particles covered and encapsulated by GNs.

Based on the XRD, Raman, and SEM analysis, it can be seen that the graphite structure changed significantly during P-milling. The chemical reactivity of graphite could be enhanced significantly by mechanical milling [40,41]. The reactivity has been analyzed quantitatively by conducting oxidation tests and determining the extent of oxidation as a function of temperature. Fig. 4 shows the
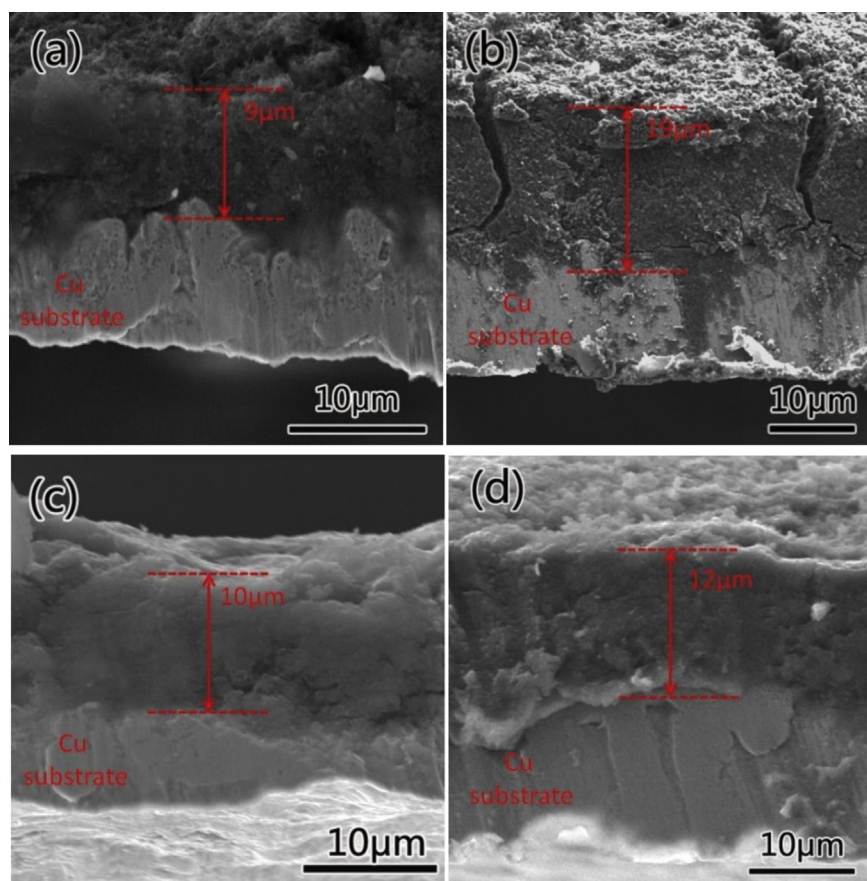

Fig. 7. The cross sectional images of (a) pristine P-0h electrode, (b) P-0h electrode after 10 cycles, (c) pristine P-20h electrode, (b) P-20h electrode after 10 cycles.

DSC curves of the P-0h, P-5h, P-10h, and P-20h samples. Graphite was oxidized at approximately 850 °C in the P-0h sample and this oxidation temperature decreased to 695 °C after 5h of P-milling. The exothermic peak in P-10h decreased to 633 °C and began to show a signal of separation. The P-20h showed two separate exothermic peaks at approximately 563 °C and 625 °C, which is attributed to the graphite having two different types of structure in the P-20h sample. The peak at 563°C originates from the oxidation of a large amount of high activity GNs, while the 625 °C peak is attributed to residual graphite which has been reduced to micro-sized pieces. The inflection point at approximately 587 °C in the TG curve of the P-20h sample (Fig. 4, inset) separates the curve into two parts with different rates of mass loss. By combining these results with those from the DSC curve of the P-20h sample, it can be seen that the first part ranges from approximately 500 °C–587 °C with a mass loss of 40% being attributed to the *in-situ* formation of GNs in the P-20h composite.

TEM and high resolution TEM was conducted to observe the distribution of nano-Si particles in the GNs matrix and the detailed features of GNs in the P-20h sample. As shown in Fig. 5a, nano-Si particles were dispersed uniformly in the GNs, which were entangled with one other. Fig. 5b shows an enlargement of the zone delineated by the dotted circle in Fig. 5a, and it can be seen clearly that the nano-Si particles are enclosed in the GNs. Arrow A (Fig. 5c) shows that the GN thickness is 7–8 nm and corresponds to approximately 20 layers of stacking of the monatomic graphene sheets. These results are consistent with the XRD results in Table 1. Thinner GNs with a thickness of only 2–3 nm were also present as indicated by arrow B. A schematic diagram (Fig. 5d, inset) for the cutting effect of nano-Si particles shows that graphene layers were peeled from the microsized graphite surface by rigid nano-Si particles. This indicates how nano-Si particles can act as nanomillers and why silicon bonds strongly with the GNs. This should ensure the enhanced performance of the P-20h nano-Si/GNs composite.

Fig. 6a shows the cycle performances of the P-5h, P-10h, and P-20h nano-Si/graphite composite electrodes in half cells at 200 mAg^{-1} between 0.01 and 1.5 V. The nano-Si and P-0h anodes were also tested for comparison. The capacity of the nano-Si anode decreased to approximately 30 mAhg^{-1} after 6 cycles, confirming the poor cycle performance of pure Si even when 50–100 nm in size. The unmilled P-0h sample delivered a high initial discharge capacity of 867 mAhg^{-1} but this decreased to 194 mAhg^{-1} after 50 cycles. In contrast, after treatment by P-milling, the P-5h sample delivered a discharge capacity of 1050 mAhg^{-1} in the first cycle with much higher capacities being retained in subsequent cycles than the P-0h sample. Improved cycleabilities and capacities could be achieved when using the P-10h and especially the P-20h sample. The P-20h sample delivered a capacity of 1184 mAhg^{-1} during the first cycle and a reversible capacity of 715 mAhg^{-1} after 50 cycles. P-milling treatment for 20 h can therefore enhance the electrochemical performance of the nano-Si/graphite composites anode in LIBs. This behavior is attributed firstly to a sufficient P-milling time to produce abundant GNs and secondly to the fact that the nano-Si particles can be more homogenously dispersed and embedded in the GNs while leaving homogenous nanosized free spaces in the composite. These spaces can alleviate large volume changes for the lithiation/delithiation of nano-Si particles, improve their conductivity and prevent agglomeration.

Fig. 6b shows Nyquist plots of nano-Si and the P-20h nano-Si/GNs composite. Both samples were tested after the first charge–discharge cycle at 1.5 V. According to previous studies [27,31], the semicircle in the medium-frequency region is attributed to charge-transfer resistance and the inclined line in the low frequency range corresponds to lithium diffusion in the electrodes. This means that the nano-Si anode has a large resistance to charge

transfer. However, with highly conductive GNs coatings, the charge transfer resistance is reduced in the P-20h nano-Si/GNs composite anode. According to the current versus voltage curves of the bulk composite samples in Fig. 6c, P-20h has a resistance of 5 Ω (corresponding to a resistivity of 0.33 Ωm), while the resistance of the nano-Si is higher at 6.77×10^7 Ω (resistivity of 4.49×10^6 Ωm). The GNs which were produced *in-situ* during P-milling could enhance the intrinsic conductivity of the Si-based composite.

Fig. 7 shows the typical cross sectional images of the P-0h and the P-20h electrode before and after 10 cycles. The thickness of P-0h electrode before cycling was about 9 μm, and it increased to about 19 μm after cycling (Fig. 7(a) and (b)). And there are also some cracks grow in the P-0h electrode after cycling. In striking contrast, as displayed in the Fig. 7(c) and (d), the P-20h electrode did not show such significant changes before and after cycling as the P-0h electrode. The thickness of P-20h electrode had a small increase of 2 μm and no obvious cracks after 10 cycles. These results provided good evidence that the P-20h composite with a unique structure of nano-Si dispersed and embedded in the GNs which cloud buffer the volume expansion of Si and keep the integrity of whole electrode during the cycling.

The P-20h nano-Si/GNs composite has a better balance between high reversible capacity and good cycle performance and its charge–discharge behavior was therefore investigated further. Fig. 8a shows the initial five CV curves of the P-20h sample in a half cell.
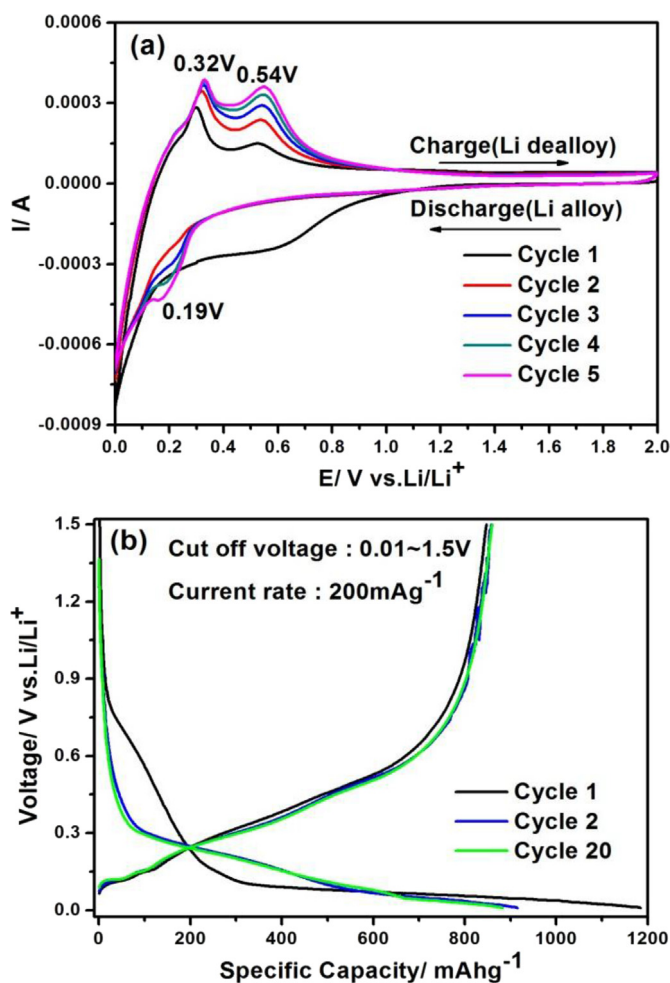

Fig. 8. (a) CV curves of P-20h nano-Si/GNs composite sample from 0.01 to 2.0 V at a scanning rate of 0.3 mVs^{-1}. (b) Charge-discharge curves for the first, second, and twentieth cycles of P-20 nano-Si/GNs composite at 200 mAg^{-1} between 0.01 and 1.5 V.

The broad reductive peak at approximately 0.7 V versus Li/Li⁺ is only observed in the first cathodic scan and disappears from the second cycle. This is attributed to the irreversible reduction of electrolyte and the formation of a solid electrolyte interphase (SEI) film on the anode. The other two cathodic peaks at approximately 0.19 V and below 0.1 V versus Li/Li⁺ are attributed to Li−Si alloy formation. Correspondingly, the anodic peaks at approximately 0.32 and 0.54 V versus Li/Li⁺ are related to the decomposition of the Li−Si phases. This indicates that the nano-Si is the dominant reactant with lithium in the P-20h nano-Si/GNs composite.

Fig. 8b displays the charge−discharge curves for the first, second, and twentieth cycles of the P-20h nano-Si/GNs composite electrode. In the first cycle, the P-20h electrode shows an initial discharge and charge capacity of 1184 and 847 mAhg⁻¹, respectively, corresponding to an initial coulombic efficiency of 71.6% and an irreversible capacity loss of 337 mAhg⁻¹. The irreversible capacity loss in the first cycle occurs mainly because of the formation of an SEI film in the high surface area of the GNs at 0.7 V [31,42]. Li⁺ consumption occurs because the crystalline silicon is converted to amorphous silicon in the low potential zone [43] and needs to be reduced by further microstructure tuning of the active Si. For the second and twentieth cycles, the discharge/charge capacities of the P-20h electrode were 915/858 and 876/856 mAhg⁻¹, respectively. The charge/discharge efficiency increased to 94% in the second cycle and reached 98% in the twentieth cycle. The discharge−charge curves almost overlap from the second to twentieth

cycle and confirm the good reversibility in reaction of the nano-Si/GNs composite electrode.

Fig. 9a shows the discharge capacity versus cycle number for the P-20h nano-Si/GNs composite half cells at current rates of 50, 100, and 400 mAg⁻¹. There was a significant improvement in cycleability with higher capacity at lower current rates. The cell cycling at a current rate of 50 mAg⁻¹ maintained a stable reversible capacity of 976 mAhg⁻¹ after 50 cycles. As the current rates increase to 100 and 400 mAg⁻¹, after 50 cycles, the electrode can deliver a stable reversible capacity of 853 and 723 mAhg⁻¹, which is 87% and 74% of that at the current rate of 50 mAg⁻¹, respectively. The superior cycle stability and high rate capability of the P-20h nano-Si/GNs composite could be attributed to the enhanced structural stability and conductivity of the electrodes resulting because most of the nano-Si particles are embedded in the highly conductive and fixable GNs matrix. The practical application of the nano-Si/GNs composite anode was further tested in a coin-type full cell using a LiMn₂O₄ cathode. The cycle performance of the full cell is shown in Fig. 9b. The cell delivers a specific capacity of approximately 600 mAhg⁻¹ for the P-20h anode with good capacity retention over 30 cycles at a constant current rate of 400 mAg⁻¹ (based on anode, approximately 0.5 C). The charge/discharge curves (inset) reveal that the practical working voltage of the full cell lies between 3.0 and 4.0 V, with average discharge and charge voltages of 3.6 and 4.0 V, respectively. The nano-Si/GNs composite anode therefore maintains a high working voltage compared with that of a graphite
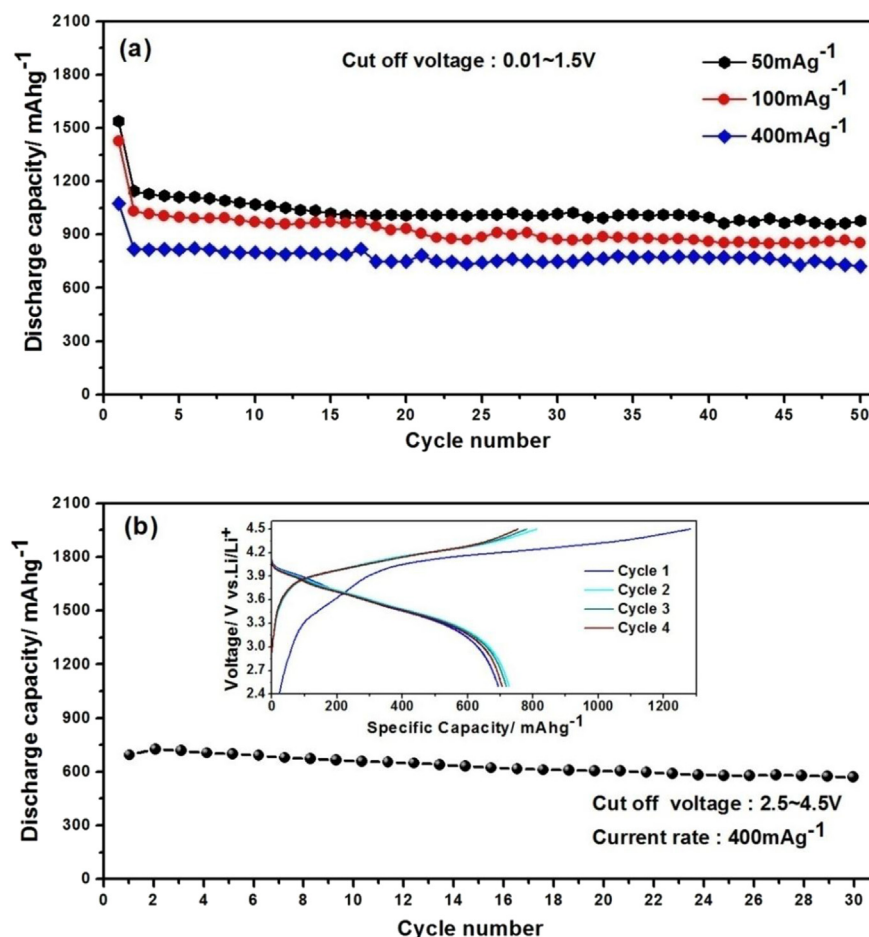

Fig. 9. (a) Cycle performance of P-20h nano-Si/GNs composite at current rates of 50, 100 and 400 mAg⁻¹ between 0.01 and 1.5 V. (b) Discharge capacity versus cycle number for full cell using LiMn₂O₄ cathode and P-20h nano-Si/GNs composite anode at 400 mAg⁻¹ between 2.5 and 4.5 V. Inset shows charge−discharge curves for first to fourth cycle of full cell.

anode. However, the P-20h composite anode in the full cell delivers a lower capacity of approximately 150 mAhg^{-1} than that in the half cell. This occurs mostly because the commercial LiMn$_2$O$_4$ cathode cannot provide sufficient Li$^+$ for the reaction at a current rate of approximately 0.5 C. The electrochemical performance of the nano-Si/GNs composite could be further optimized by tuning the material composition (with higher Si content and using microsized Si), nanostructure, and P-milling process. These factors are being investigated and will be reported on in future.

4. Conclusions

In summary, nano-Si/GNs composite anode materials have been produced by discharge plasma-assisted milling. Graphene nanosheets could easily be peeled off from the graphite by the cutting effect of the Si nanomiller, milling balls and thermal explosion of the discharge plasma. The nano-Si/GNs composite, which was treated by P-milling for 20 h, possessed a unique structure of nano-Si particles embedded homogeneously among the graphene nanosheets along with an abundance of nanosized free spaces. This enhanced the anode conductivity and cycle performance in lithium–ion batteries. The synthetic route developed in this work is simple, low-cost, and pollution-free and can be adopted for large-scale production of Si/graphene-based composite anodes.

Acknowledgments

References

[1] J.-M. Tarascon, M. Armand, Nature 414 (2001) 359–367.
[2] P.G. Bruce, B. Scrosati, J.M. Tarascon, Angew. Chem. 47 (2008) 2930–2946.
[3] A. Shukla, T. Prem Kumar, Curr. Sci. 94 (2008) 314–331.
[4] M. Winter, J.O. Besenhard, M.E. Spahr, P. Novak, Adv. Mater. 10 (1998) 725–763.
[5] M. Winter, J.O. Besenhard, Electrochim. Acta 45 (1999) 31–50.
[6] B. Boukamp, G. Lesh, R. Huggins, J. Electrochem. Soc. 128 (1981) 725–729.
[7] T. Hatchard, J. Dahn, J. Electrochem. Soc. 151 (2004) A838–A842.
[8] C.K. Chan, H. Peng, G. Liu, K. McIlwrath, X.F. Zhang, R.A. Huggins, Y. Cui, Nat. Nanotechnol. 3 (2007) 31–35.
[9] Y. Yu, L. Gu, C. Zhu, S. Tsukimoto, P.A. van Aken, J. Maier, Adv. Mater. 22 (2010) 2247–2250.
[10] G. Wang, J. Yao, H. Liu, Electrochem. Solid-State Lett. 7 (2004) A250–A253.
[11] T. Cetinkaya, M. Guler, H. Akbulut, Microelectron. Eng. 108 (2013) 169–176.
[12] Z. Guo, E. Milin, J. Wang, J. Chen, H. Liu, J. Electrochem. Soc. 152 (2005) A2211–A2216.
[13] W. Wang, P.N. Kumta, ACS Nano 4 (2010) 2233–2241.
[14] A. Wilson, J. Dahn, J. Electrochem. Soc. 142 (1995) 326–332.
[15] S. Cahen, R. Janot, L. Laffont-Dantras, J.-M. Tarascon, J. Electrochem. Soc. 155 (2008) A512–A519.
[16] M. Holzapfel, H. Buqa, F. Krumeich, P. Novak, F.-M. Petrat, C. Veit, Electrochem. Solid-State Lett. 8 (2005) A516–A520.
[17] S. Chew, Z. Guo, J. Wang, J. Chen, P. Munroe, S. Ng, L. Zhao, H. Liu, Electrochem. Commun. 9 (2007) 941–946.
[18] H. Kim, J. Cho, Nano Lett. 8 (2008) 3688–3691.
[19] J. Shu, H. Li, R. Yang, Y. Shi, X. Huang, Electrochem. Commun. 8 (2006) 51–54.
[20] X. Du, P. Guo, H. Song, X. Chen, Electrochim. Acta 55 (2010) 4812–4819.
[21] S. Park, R.S. Ruoff, Nat. Nanotechnol. 4 (2009) 217–224.
[22] L. Ji, Z. Lin, M. Alcoutlabi, X. Zhang, Energy & Environ. Sci. 4 (2011) 2682–2699.
[23] L. Ji, H. Zheng, A. Ismach, Z. Tan, S. Xun, E. Lin, V. Battaglia, V. Srinivasan, Y. Zhang, Nano Energy 1 (2012) 164–171.
[24] I.-Y. Jeon, Y.-R. Shin, G.-J. Sohn, H.-J. Choi, S.-Y. Bae, J. Mahmood, S.-M. Jung, J.-M. Seo, M.-J. Kim, D.W. Chang, Proc. Natl. Acad. Sci. 109 (2012) 5588–5593.
[25] K.S. Novoselov, A.K. Geim, S. Morozov, D. Jiang, Y. Zhang, S. Dubonos, I. Grigorieva, A. Firsov, Science 306 (2004) 666–669.
[26] S. Bae, H. Kim, Y. Lee, X. Xu, J.-S. Park, Y. Zheng, J. Balakrishnan, T. Lei, H.R. Kim, Y.I. Song, Nat. Nanotechnol. 5 (2010) 574–578.
[27] H. Xiang, K. Zhang, G. Ji, J.Y. Lee, C. Zou, X. Chen, J. Wu, Carbon 49 (2011) 1787–1796.
[28] E. Yoo, J. Kim, E. Hosono, H.-s. Zhou, T. Kudo, I. Honma, Nano Lett. 8 (2008) 2277–2282.
[29] H. Wu, W. Zhao, H. Hu, G. Chen, J. Mater. Chem. 21 (2011) 8626–8632.
[30] M.J. McAllister, J.-L. Li, D.H. Adamson, H.C. Schniepp, A.A. Abdala, J. Liu, M. Herrera-Alonso, D.L. Milius, R. Car, R.K. Prud'homme, Chem. Mater. 19 (2007) 4396–4404.
[31] S.-L. Chou, J.-Z. Wang, M. Choucair, H.-K. Liu, J.A. Stride, S.-X. Dou, Electrochem. Commun. 12 (2010) 303–306.
[32] H. Liu, R. Hu, M. Zeng, J. Liu, M. Zhu, J. Mater. Chem. 22 (2012) 8022–8028.
[33] H. Liu, R. Hu, W. Sun, M. Zeng, J. Liu, L. Yang, M. Zhu, J. Power Sources 242 (2013) 114–121.
[34] L. Dai, B. Cao, M. Zhu, Acta Metall. Sin. (English Letters) 19 (2006) 411–417.
[35] M. Zhu, L. Dai, N. Gu, B. Cao, L. Ouyang, J. Alloys Compd. 478 (2009) 624–629.
[36] K. Fukuda, K. Kikuya, K. Isono, M. Yoshio, J. Power Sources 69 (1997) 165–168.
[37] T. Xing, L.H. Li, L. Hou, X. Hu, S. Zhou, R. Peter, M. Petravic, Y. Chen, Carbon 57 (2013) 515–519.
[38] A. Ferrari, J. Robertson, Phys. Rev. B 61 (2000) 14095.
[39] A. Ferrari, J. Robertson, Phys. Rev. B 64 (2001) 075414.
[40] H. Harker, J. Horsley, D. Robson, Carbon 9 (1971) 1–9.
[41] H. Hermann, T. Schubert, W. Gruner, N. Mattern, Nanostruct. Mater. 8 (1997) 215–229.
[42] G. Wang, X. Shen, J. Yao, J. Park, Carbon 47 (2009) 2049–2053.
[43] M.N. Obrovac, L.J. Krause, J. Electrochem. Soc. 154 (2007) A103.